Strathprints Institutional Repository

Journal Name

ARTICLE TYPE

Combining Random Forest and 2D Correlation Analysis to identify serum spectral signatures for neuro-oncology†

Benjamin R. Smith,[a,b] Katherine M. Ashton,[c] Andrew Brodbelt,[d] Timothy Dawson,[c] Michael D. Jenkinson,[d] Neil T. Hunt,[e] David S. Palmer,[*a] and Matthew J. Baker[*b]

Fourier transform infrared (FTIR) spectroscopy has long been established as an analytical technique for the measurement of vibrational modes of molecular systems. More recently, FTIR has been used for the analysis of biofluids with the aim of becoming a tool to aid diagnosis. For the clinician, this represents a convenient, fast, non-subjective option for the study of biofluids and the diagnosis of disease states. The patient also benefits from this method, as the procedure for the collection of serum is much less invasive and stressful than traditional biopsy. This is especially true of patients in whom brain cancer is suspected. A brain biopsy is very unpleasant for the patient, potentially dangerous and can occasionally be inconclusive. We therefore present a method for the diagnosis of brain cancer from serum samples using FTIR and machine learning techniques. The scope of the study involved 433 patients from whom were collected 9 spectra each in the range 600-4000 cm^{-1}. To begin the development of the novel method, various pre-processing steps were investigated and ranked in terms of final accuracy of the diagnosis. Random Forest machine learning was utilised as a classifier to separate patients into cancer or non-cancer categories based upon the intensities of wavenumbers present in their spectra. Generalised 2D correlational analysis was then employed to further augment the machine learning, and also to establish spectral features important for the distinction between cancer and non-cancer serum samples. Using these methods, sensitivities of up to 92.8% and specificities of up to 91.5% were possible. Furthermore, ratiometrics were also investigated in order to establish any correlations present in the dataset. We show a rapid, computationally light, accurate, statistically robust methodology for the identification of spectral features present in differing disease states. With current advances in IR technology, such as the development of rapid discrete frequency collection, this approach is of importance to enable future clinical translation and enables IR to achieve its potential.

[a] WestCHEM, Department of Pure and Applied Chemistry, University of Strathclyde, Thomas Graham Building, 295 Cathedral Street, Glasgow, Scotland G1 1XL, United Kingdom; E-mail: david.palmer@strath.ac.uk

[b] WestCHEM, Department of Pure and Applied Chemistry, University of Strathclyde, Technology and Innovation Centre, 99 George Street, Glasgow G1 1RD, United Kingdom; E-mail: matthew.baker@strath.ac.uk

[c] Neuropathology, Lancashire Teaching Hospitals NHS Trust, Royal Preston Hospital, Sharoe Green Lane, Fulwood, Preston, PR2 9HT, United Kingdom.

[d] Neurosurgery, The Walton Centre NHS Foundation Trust, Lower Lane, Fazakerley, Liverpool, L9 7LJ, United Kingdom.

[e] SUPA, Department of Physics, University of Strathclyde, 107 Rottenrow East, Glasgow,

1 Introduction

Cancer is a leading cause of death and ill health across the modern world. Approximately 14 million new cases and 8.2 million deaths attributed to cancer occurred in 2012.[1] It is important that we have methods to quickly and easily diagnose types of cancer, to ensure the best treatment is provided for patients. Among all types of cancer, brain tumours stand out as a particular challenge to treat effectively. This category of cancer is one of the few which have a higher mortality than incidence rate. For example, in the UK in 2006-2010 brain cancer had an incidence of 18% among young cancer sufferers, but accounted for 34% of mortality.[2] Despite the relatively high incidence of brain cancer in general, its causes are not fully understood, though some have been identified.[3] Malignant gliomas cause on average a 20-year reduction in life expectancy[4] and among those, high grade Glioblastoma Multiforme (GBM) represents a particularly bleak outcome with just 6% of adults surviving more than 5 years after diagnosis.[5] There are two main classes of brain tumour, namely primary and secondary brain tumours. The distinction between these two is the location in the body from which the cancer originated. Primary tumours (e.g. GBM) originate from within the central nervous system (CNS), with gliomas originating from the tissue which surrounds and supports the neurons in the brain, i.e. glial cells.[6] Secondary (metastatic) tumours originate from elsewhere in the body, and are transported to the brain. In the UK, around 13,000 people are diagnosed annually with brain cancer[7], of which about 67% are secondary tumours.[8] Of these secondary tumours, the breakdown of origins is as follows: Lung (50%), breast (15-25%), skin (melanoma) (5-20%) and all others (5-30%).[9] By identifying the organ of origin, treatment efficiency and patient survival can be increased, but the primary location is unknown in around 15% of metastatic cases.

Current diagnostic methods are time consuming, expensive and require highly skilled practitioners to interpret them. In the case of brain and CNS cancers, the test usually consists of an MRI or CT scan in the first instance.[10] These types of complex results can be subjective in their conclusions. (The CT scan itself has disputed health risks.[11,12]) In some cases, these tests prove to be inconclusive, and warrant further investigation. Upon such an occurrence a biopsy of the suspected tumour is indicated. A biopsy of brain tissue represents an invasive and stressful procedure for patients, again needing highly skilled surgical and pathological expertise. Even when a biopsy is taken, there can be discrepancies in the interpretation of results between medics. Bruner *et al.* found that of 500 biopsy cases, 214 (42.8%) had a degree of disagreement between original and review diagnoses.[13] In England in the period 2006-2010, 54% of cancer cases were diagnosed following a routine or urgent GP referral, either as part of the "two week wait" system or otherwise.[14] The two-week wait system is an urgent referral (less than two weeks of waiting time for a consultation) of a patient to a specialist, should cancer be suspected by a GP. However, 23% of cancer cases in England during this time period were diagnosed after presenting as an emergency.[14] Concentrating on brain and CNS cancers, the National Cancer Intelligence Network (NCIN) statistics show that more than half (58%) of brain and CNS cancers are diagnosed through presentation at emergency facilities, with the "two week wait" system only accounting for 1% of the total.[15] In these later diagnoses, prognosis is much poorer for all types of cancer. As well as having on average a later secondary care diagnosis, brain tumours are very difficult to identify in primary care and a high index of suspicion is required. A survey carried out on behalf of The Brain Tumour Charity (UK) found that 38% of people living with a brain tumour had visited their GP more than 5 times before being diagnosed.[16] Overall, the current system for the detection and diagnosis of brain tumours in general is not satisfactory. A reliable, fast and simple method to screen for these types of cancer would reduce time before diagnosis and therefore increase survival rates, as many therapies are more effective when started early.

IR spectroscopy has previously been investigated as a cancer diagnosis tool. Haka *et al.* showed the merit of human tissue spectroscopy in distinguishing breast tumours from normal tissue.[17] Laboratory based proof of principle studies have shown the ability of serum spectroscopy to diagnose cancerous disease states, such as those reviewed by Kondepati *et al.*[18] Pichardo *et al.* were also able to use spectroscopy together with machine learning to detect breast cancer.[19] Most of these investigations in the literature focus on very specific types of cancerous diseases states, or require tissue samples from suspected tumours to aid in diagnosis. A broader approach based on IR spectroscopy of serum samples could be an ideal solution. Serum can be acquired from blood samples in a much less invasive procedure. Backhaus and Mueller *et al.* demonstrated a method to successfully detect breast cancer using serum samples and IR spectroscopy. The sensitivity and specificity achieved were 98% and 95% respectively.[20] Gajjar *et al.* used FTIR of serum and plasma samples to distinguish ovarian and endometrial cancer patients from control patients.[21] They used various feature extraction methods to obtain very promising results from a small pilot study. Ovarian cancer was detectable with 95% correct classification.

Our previous research has shown the ability of combined FTIR and machine learning to identify differing levels of cytokine and angiogenesis factors in patients with glioma.[22] The Bioplex study provided sensitivities and specificities as high as 88% and 81% respectively. Furthermore, sensitivities and specificities of 87.5%

and 100% were achieved when combining ATR-FTIR with Support Vector Machines (SVM). A similar approach was employed to distinguish differing grades of glioma (high-grade and low-grade) from non-cancer.[6] Sensitivity and specificity were 93.75% and 96.53% respectively.

We now build on our previous diagnostic research[6,22–25] with a larger dataset, a different approach to machine learning and the technique of generalised 2D correlational analysis. Some studies have used "black box" machine learning.[22,26] While this can give good predictions, it does not give full insight into the actual features being used for classification, which in turn does not aid clinical translation. In order to translate novel technologies to the clinic, further information is required to identify spectral peaks that provide diagnostic information. In addition, identifying relevant features will enable future rapid collection protocols via techniques such as Quantum Cascade Laser IR spectroscopy.[27,28] Focusing on the salient information of a spectral dataset also provides enhanced diagnostic accuracy due to the removal of extraneous information that is clouding the diagnosis based upon biological variance. Dorling and Baker[29] describe the utility of serum spectroscopy in the clinic, in order to achieve this we have to provide rapid, accurate and information-rich analysis to correctly describe the difference in disease state molecular species.

IR spectroscopy of biological materials is not straightforward. Serum itself is a very complex mixture of various components. In addition to the chemical complexity of serum, optimum sample preparation techniques and their effect on the spectrum are not known. The group has therefore established guidelines by means of a dilution study coupled with a comparison of ATR-FTIR and High Throughput (HT)-FTIR.[30] It was found that 3-fold dilution was optimal for HT-FTIR in terms of scores in a spectral quality test. ATR-FTIR although slower than HT-FTIR, proved to be the best when investigating discernible features. Also previously established by the group was the optimum drying time of 8 minutes.[6]

Generalised 2D correlation spectroscopy is a data analysis method developed by Noda[31], as distinct from ultrafast 2D-IR spectroscopy, which measures vibrational couplings in an analogous way to 2D-NMR.[32] Noda's generalised method allows external perturbations (temperature, concentration, pH etc) to be used to obtain information about the effect of external influences on spectra, and does so by offering two main types of correlation which are synchronous and asynchronous. Synchronous spectra represent coinciding changes in different spectral regions. The synchronous spectrum is symmetrical, and contains peaks (called autopeaks) along the diagonal. The strength of the highlighted areas along this line represent the band strength of the IR regions. Peaks off the diagonal (called cross-peaks) show correlation between underlying 1D spectral peaks. If the sign is positive (blue in this work), then both 1D peaks are changing in the same direction, either increasing or decreasing in intensity. Negative signs (red) show that the 1D spectral peaks are moving in opposite directions in terms of intensity. Asynchronous spectra represent sequential changes in the 1D spectra due to the perturbation. When a cross-peak is of a positive sign, then a peak from the first spectrum is changing before a band from the second spectrum, and vice versa. A feature of these asynchronous spectra is that they contain no autopeaks, and are anti-symmetric with respect to the diagonal.

The type of machine learning used in this work (Random Forest) is interpretable, and results in a better understanding of the relative importance of distinguishing features. Furthermore, we combine this method with 2D correlational analysis. The novel combination of these usually disparate methods allows for both the building of an accurate classifier, and the characterisation of spectral features important for diagnosis.

2 Materials and Methods

2.1 Spectral Collection

The research described in this paper was performed with full ethical approval (Walton Research Bank BTNW/WRTB 13_01/BTNW Application #1108). The dataset consists of IR data from serum samples of 433 patients with differing brain cancer diagnoses taken at the Royal Preston Hospital, in conjunction with Brain Tumour North West. The entire dataset comprises 9 spectra for each patient. These 9 spectra were generated from 3 IR passes of 3 separate sample preparations. Each sample of $1\mu L$, was allowed to dry for 8 minutes before spectra were collected. Data was gathered using an Agilent Cary-600 Series FTIR spectrometer with a PIKE Technologies MIRacle^{TM}single-reflection ATR utilising a diamond crystal plate. Spectra were subject to Agilent Resolutions ATR correction. Spectra were obtained in the range 600-4000 cm^{-1}, with a resolution of 1.926 cm^{-1}. All samples had been frozen before spectral collection, and defrosted immediately prior to the measurement. Figure 1 shows the organisation of the dataset, while Table 1 shows the number of patients per disease category.

**Table 1** Breakdown of patient numbers according to disease state

Disease State	Number of Patients
Cancer	311
Non-Cancer	122
Primary Brain Cancer	134
Metastatic Brain Cancer	177
High Grade Glioma	64
Low Grade Glioma	23

Fig. 1 Hierarchical categories of disease states
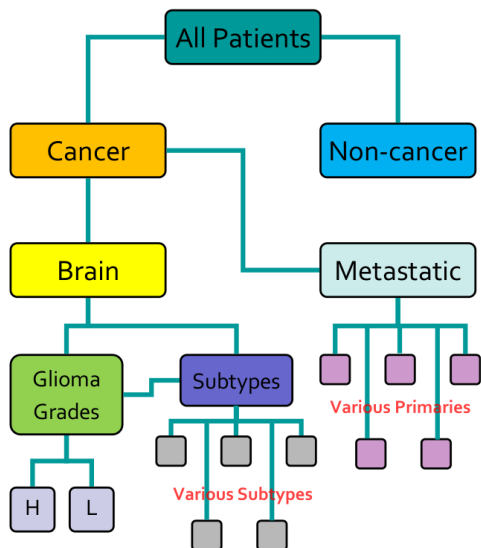
Fig. 2 All spectra with various pre-processing. Red - raw data, magenta - normalised spectra, green - normalised first derivative and blue - normalised second derivative.
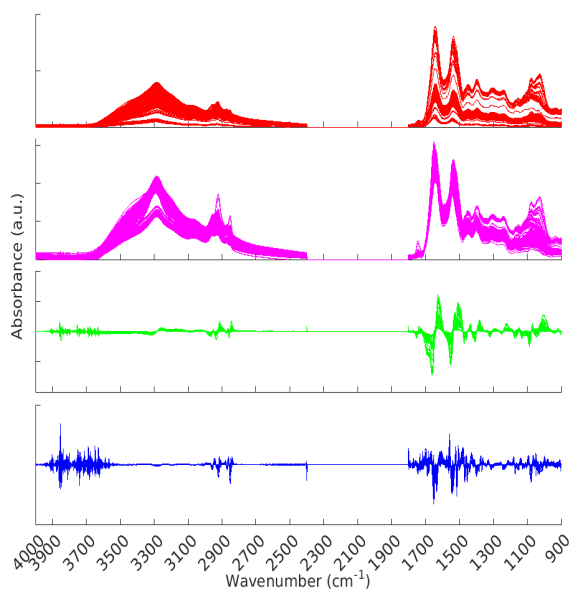
2.2 Pre-processing

All pre-processing was undertaken using Matlab.[33] All spectra were vector normalised, and optionally a first or second derivative taken using 5 smoothing points (Savitzky-Golay method). During the pre-processing phase, any spectra displaying gross spectral error were discarded. These erroneous spectra amounted to 2

whole patients(18 spectra) and 7 other spectra, for a total of 25 spectra being removed. One of the patients for which all spectra were erroneous was from the Metastatic Brain Cancer group, and the other from the Low Grade Glioma group. For the analysis this left 309, 176 and 22 patients in the Cancer, Metastatic and Low Grade Glioma groups respectively. Other types of pre-processing were tried; (raw data and first derivative, both with or without normalisation) and the normalised second derivative with 5 smoothing points was found to be the best in terms of statistical results and clarity of Random Forest Gini importance peaks. (See section 2.5 for explanation of Gini importance.) The data was split into two sections after the removal of the CO_2 region. The regions considered were 900-1800 cm^{-1} and 2400-4000 cm^{-1}. See Figure 2 for an overview of the the spectra during pre-processing. Figure S1 in the E.S.I. shows averaged cancer and non-cancer spectra together with standard deviations for each.

2.3 Ratios

Ratios of ranges of wavenumbers were taken from the raw spectral data, after removal of erroneous spectra. These were calculated using a simple sum of intensities of the relevant regions of the spectra. Ratios such as these have been previously shown to be important in diagnosis of various diseases from IR spectra. Choice of wavenumber ranges was steered by previous literature, as well as wavenumber ranges found to be important to our machine learning classification. Ratios in the range 1030-1080 relating to glycogen and phosphate vibrations, are thought[34] to be useful in distinguishing malignant and non-malignant disease states. Ratios 3160:3170 and 3190:3200 were found by Bassan *et al.*[35] to be leading discriminatory metrics in malignant breast cancer detection. The ratio listed as "Navarro" was investigated in order to obtain protein:lipid ratios for the spectra as suggested by Navarro *et al.*[36] Another protein:lipid ratio was also investigated, this was established by Baker *et al.*[37] as a protocol. Furthermore, we consider ratios BRS1-4 which were chosen from regions important for the classification of cancer/non-cancer which became apparent from preliminary RF models.

Table 2 Ratios investigated for correlation

Ratio ID	Wavenumbers	Regions
1030:1050	1030:1050	Carb.
1030:1080	1030:1080	Carb.-Phos.
1050:1080	1050:1080	Phos.
3160:3170	3160:3170	Alcohols
3190:3200	3190:3200	O–H–O
Navarro	$\Sigma(1650\text{-}1700){:}\Sigma(1730\text{-}1800)$	Protein:Lipid
Baker	many‡	Protein:Lipid
BRS 1	$\Sigma(1600\text{-}1680){:}\Sigma(1500\text{-}1580)$	AmideI:AmideII
BRS 2	$\Sigma(1220\text{-}1280){:}\Sigma(1380\text{-}1420)$	Phos.A:COO$^-$
BRS 3	$\Sigma(1000\text{-}1050){:}\Sigma(1430\text{-}1470)$	Carb.:CH$_2$
BRS 4	$\Sigma(1000\text{-}1050){:}\Sigma(2830\text{-}3000)$	Carb.:CH$_2$,CH$_3$

2.4 Random Forest

The main method employed for classification in this study was Random Forest(RF),[38] as implemented in R. The specific package used was randomForest, by Liaw and Wiener.[39] This is a machine learning method used to find features associated with input classes. From the training set, RF builds a "forest" of regression trees using the CART (Classification and Regression Trees) algorithm. There are three possible training parameters for Random Forest: ntree - the number of trees in the Forest; mtry - the number of different descriptors tried at each split; and nodesize - the minimum node size below which leaves are not further subdivided. In our work, the number of trees generated per classification was 500. The variable 'mtry' was one third of the number of descriptors and 'nodesize' was 5. These are the default settings for the package, and have proved to be optimal in our previous studies using randomForest.[40–42] training:test set split was 80:20, respectively. 5-fold cross validation of the training set was also carried out.

The Random Forest machine learning method (MLM) was chosen for this work for several reasons. Firstly, RF is easily scalable when compared to other MLM. This means that the same (or very similar) parameters can be used in the future with larger datasets. Secondly, RF has easily interpreted results when used with the Gini impurity metric (see section 2.5 for an explanation of the Gini metric). This meant that important distinguishing wavenumbers were clearly defined, and their relative importance was readily established. Third, RF is known for being able to robustly handle outliers in the input space. This property potentially allows classification of spectra without heavy pre-processing, whereas other MLM may require it. Finally, RF deals well with missing values from input classes. This was especially important to our work, as the wavenumber range 1800-2400 cm^{-1} was removed.

For the interpretation of the RF outcome, two main groups of results were considered. Firstly, a selection of statistical metrics were generated to give an in-depth analysis of the accuracy and reliability of each classification. These were based upon true positive(TP), true negative(TN), false positive(FP) and false negative(FN) predictions as well as "real"(actual number of positives and negatives in the dataset) positives(P) and negatives(N). The abbreviation MCC stands for Matthews Correlation Coefficient.

$$Number\ of\ Positives\ (P) = TP + FN \tag{1}$$

$$Number\ of\ Negatives\ (N) = TN + FP \tag{2}$$

$$Sensitivity = \frac{TP}{P} = \frac{TP}{(TP+FN)} \tag{3}$$

$$Specificity = \frac{TN}{N} = \frac{TN}{(TN+FP)} \tag{4}$$

$$Positive\ Precision = \frac{TP}{(TP+FP)} \tag{5}$$

$$Negative\ Precision = \frac{TN}{(TN+FN)} \tag{6}$$

$$Accuracy = \frac{(TP+TN)}{(TP+FP+FN+TN)} \tag{7}$$

$$MCC = \frac{(TP*TN)-(FP*FN)}{\sqrt{(TP+FP)(TP+FN)(TN+FP)(TN+FN)}} \tag{8}$$

$$SE_{\bar{m}} = \frac{\sigma}{\sqrt{n}} \tag{9}$$

In the statistical results tables below, TS and CV represent results for the test set and cross-validation respectively. The tolerances shown for each result are their standard errors, generated according to equation 9, where $SE_{\bar{m}}$ is the standard error of the mean (of the 96 iterations), σ is the standard deviation and n is the number of samples.

2.5 Random Forest Feature Importance

Spectral feature importance results were obtained using the combined mean decrease in Gini coefficient, with respect to wavenumbers. This allowed an easily-interpreted result to be found, and wavenumber ranges important to the classification were ascertained. The Gini impurity of a node is dependent on the probability of each possible outcome. For a single node τ in the RF classification, the Gini impurity is found by Equation 10 below, where $g(\tau)$ is the impurity of node τ, n is the total number of spectra at the node while n_A and n_B are the number of spectra belonging to class A or B respectively; i.e. Cancer or Non-cancer.

$$g(\tau) = 1 - \left(\frac{n_A}{n}\right)^2 - \left(\frac{n_B}{n}\right)^2 \tag{10}$$

Every time a node is split on a predictor (wavenumber), the Gini impurity for the two child nodes is less than the parent node. This is because the dataset is gradually being sorted into predicted classes, and becoming more homogeneous with respect to the proportion of classes A or B. When node τ is split, resulting in two child nodes υ and ϕ, the change in Gini (Δg) is found by Equation 11 where n_υ and n_ϕ are the number of spectra in nodes υ and ϕ respectively. The value of Δg is larger when a greater change in impurity occurs after the split, thus allowing for the decrease in Gini to be used as a measure of importance of a certain wavenumber.

$$\Delta g = g(\tau) - \left(\frac{n_\upsilon}{n}\right) g(\upsilon) - \left(\frac{n_\phi}{n}\right) g(\phi) \tag{11}$$

The overall Gini importance (G) of a particular spectral feature θ is found by the sum across all nodes of each tree ψ, and across

all trees in forest ω (Equation 12).

$$G(\theta) = \sum_{i=1}^{\Psi} \sum_{j=1}^{\omega} \Delta g_{i,j} \qquad (12)$$

These values are then averaged for the 96 independent classifications, to arrive at the Mean Decrease (Gini) used in the figures presented in the Results and Discussion section.

2.6 Generalised 2D correlational analysis

2D correlation plots were generated with the program 2DShige,[43] and visualised in Matlab. Utilising the method developed by Noda,[31] generalised 2D correlation plots can be produced from separate 1D IR spectra which highlight changes in these spectra due to some perturbation (in this case, the perturbation was the diagnosis of cancer or not). According to Noda's Rules[44] the synchronous spectra can (qualitatively) show whether spectral intensities at two different areas of the spectrum are changing in the same direction, i.e. whether intensities are increasing or decreasing simultaneously. If a cross-peak has a positive sign, the intensities are both changing in the same direction, and in opposite directions for a negative cross-peak. The asynchronous correlations on the other hand show the sequential order of changes in intensity. Both synchronous and asynchronous 2D plots were produced of normalised, first and second derivatives, both 900-1800 cm^{-1} and 2400-4000 cm^{-1} sections of the spectrum.

3 Results and Discussion

3.1 Random Forest Results

Results were obtained by combining the findings of 96 independent RF models, and the statistics and important wavenumber regions noted. 96 was found to be an adequate number of iterations through average convergence of test runs, the plot of which can be found in the Supplementary Information of this article. The sections of the spectrum between 900-1800 cm^{-1} and 2400-4000 cm^{-1} were utilised. These sections were used in RF both separately and together. Presented here are results using normalised, first and second derivative spectra, as described in the Pre-Processing section. All results are in terms of a binary cancer/non-cancer classification.

3.1.1 900-1800 cm^{-1}.

Test set sensitivity steadily increased when increasing numerical pre-processing from normalisation to first derivative to second derivative (Tables 3-5). Sensitivities of 90.1%, 91.8% and 92.8% were recorded for these pre-processing levels. A similar increasing pattern is observed in the cross-validation set. Test set specificity showed a much more dramatic increase in percentage when more pre-processing was applied. Values of 78.5%, 88.3% and 91.5% were observed across derivatives. A similar pattern was again observed for the cross-validation result. Overall prediction

accuracies (see Equation 7) were 86.9%, 90.9% and 92.4% for the test sets, with again cross-validation keeping to the same trend. Positive precision (Equation 5) was an area in which the classification excelled, with values of 91.8%, 95.7% and 97.0% for normalised, first derivative and second derivative respectively. Negative precision (Equation 6) was in general lower than positive precision, with test set results being 74.6%, 79.5% and 81.2%. A trend of increasing precision as higher-order derivatives were applied was again followed. Matthews correlation coefficient (Equation 8) was used as a general measure of quality of the classification, with the same trend being recorded as the other metrics across its test set values of 0.674, 0.776 and 0.811. A receiver operator curve for the second derivative analysis is available in Figure S2 of the supporting information.

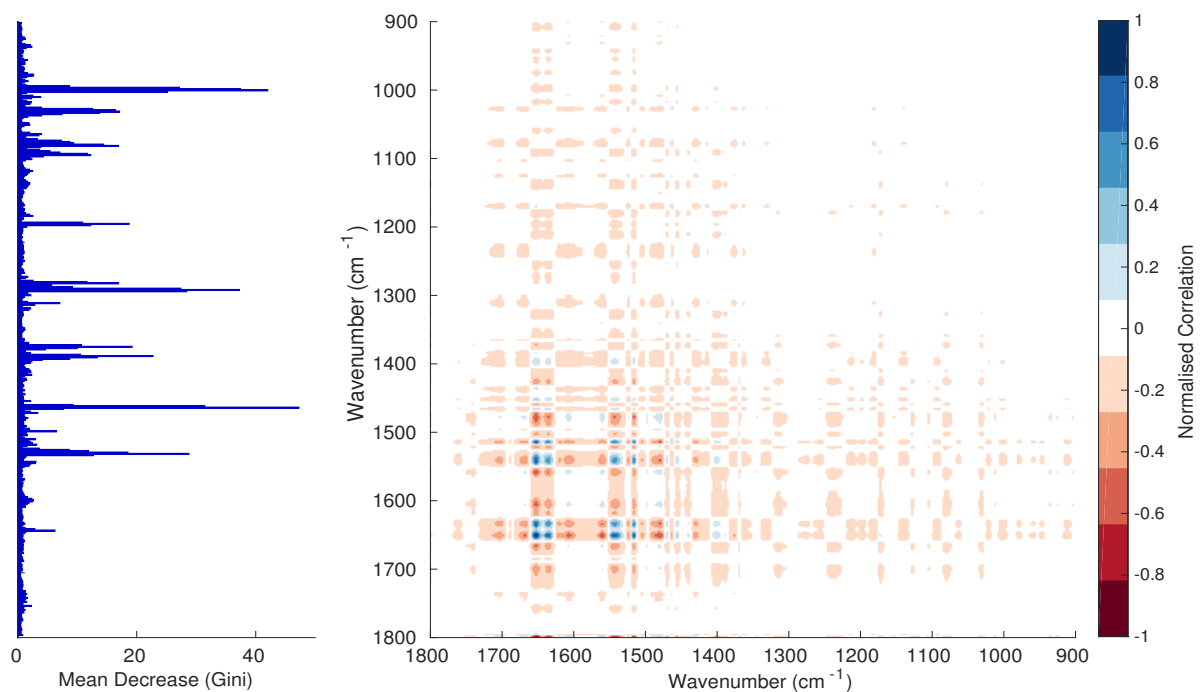### 3.1.2 2400-4000 cm^{-1}.

In general, the pattern of normalised > first derivative > second derivative did not hold for this section of the spectrum as it did for the 900-1800 cm^{-1} section. For test set sensitivity, the highest scores were recorded for the first derivative, with 87.5%, 89.7% and 82.5% found for normalised, first and second derivative respectively. Specificity (test set) followed the same pattern with 76.4%, 82.0% and 76.6%. Prediction accuracy (test set) continued the trend with 84.6%, 87.7% and 81.3% with cross-validation results being comparable. Positive precision had a different trend, this time with a score for normalised test set data of 91.6%, but the first and second derivative test sets having an equal result of 93.7%. With negative precision for the test sets, normalised data had a result of 67.7%, the first derivative a result of 73.0% and a dramatically lower score of 51.1% for the second derivative. The Matthews correlation coefficients show the general overall trend that the first derivative gives a better classification than the second derivative with this section of the spectrum, with test set results of 0.615, 0.691 and 0.513 for normalised, first derivative and second derivative respectively.

3.1.3 Both sections.

Overall, the scores and trend observed for the 900-1800 cm^{-1} section hold true for when the two sections are combined into a single classification. The metrics themselves had very similar results to this section. The only notable exception to this is the specificity metric for normalised data which did slightly better than the 900-1800 cm^{-1} section alone. Specificity for test set and cross validation set classifications were 78.5% and 76.8% for 900-1800 cm^{-1} but increased to 81.2% and 78.6% for the combined dataset.

The normalised second derivative gave the best overall accuracy according to the statistical metrics which are presented in the tables below. The first derivative results achieved a performance between normalised spectra and second derivative in terms of classification accuracy. The 2400-4000 cm^{-1} section of the spec-

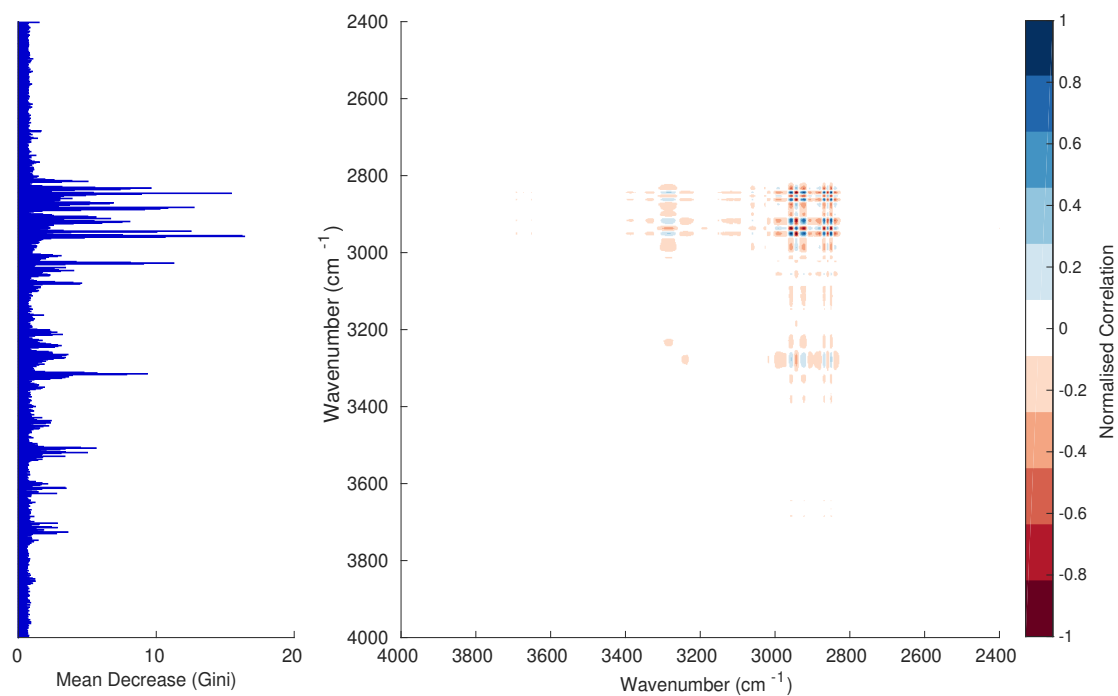**Fig. 3** Gini Importance Chart - 900-1800 cm^{-1} Second Derivative with Synchronous 2D plot

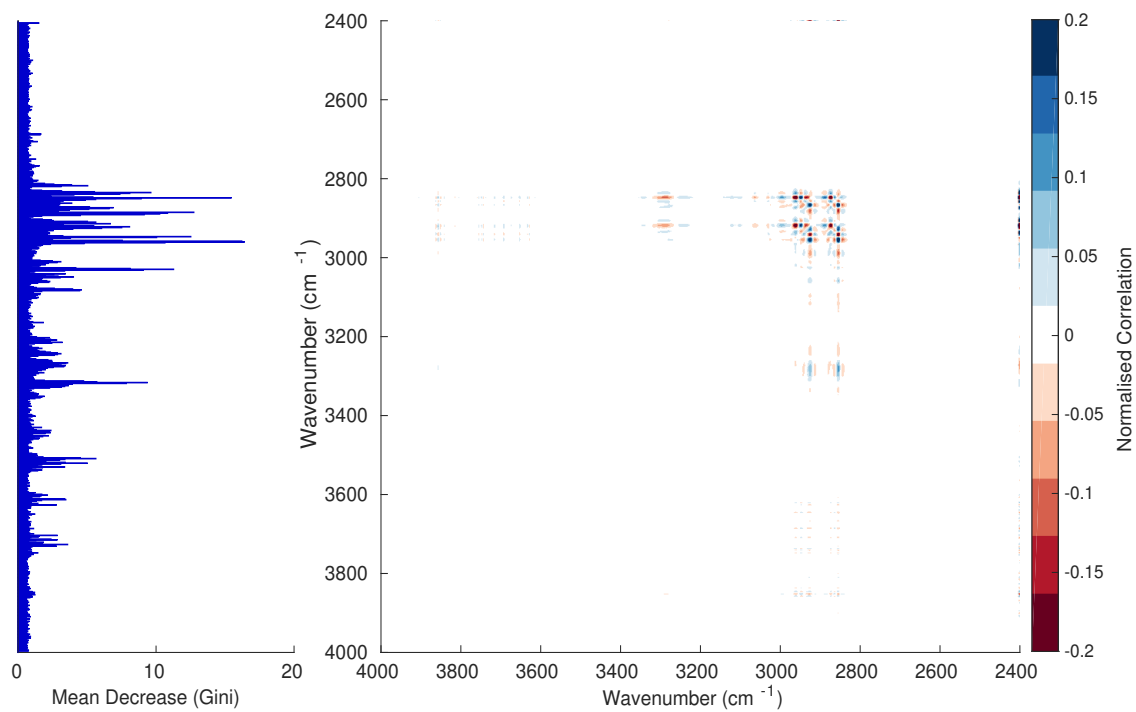**Fig. 4** Gini Importance Chart - 900-1800 cm^{-1} Second Derivative with Asynchronous 2D plot
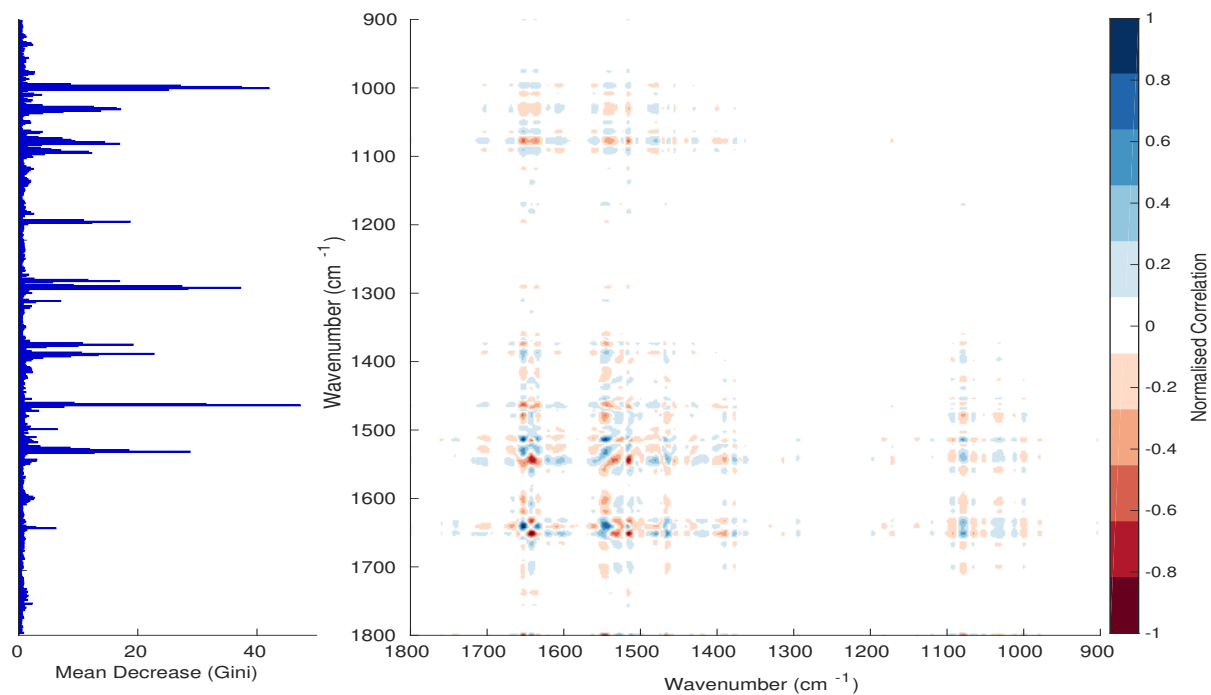
Fig. 5 Gini Importance Chart - 2400-4000 cm^{-1} Second Derivative with Synchronous 2D plot

Fig. 6 Gini Importance Chart - 2400-4000 cm^{-1} Second Derivative with Asynchronous 2D plot

trum did not perform as well as the 900-1800 cm^{-1} section, nor did it add any accuracy when these two sections were combined together.

Table 3 Statistical metrics for classification of cancer/non-cancer using RF for normalised spectra

Metric	900-1800 cm^{-1}	2400-4000 cm^{-1}	Both
Sensitivity TS	0.901±0.013	0.875±0.014	0.900±0.012
Sensitivity CV	0.899±0.006	0.872±0.007	0.897±0.006
Specificity TS	0.785±0.028	0.764±0.030	0.812±0.027
Specificity CV	0.768±0.014	0.733±0.016	0.786±0.014
Prediction Accuracy TS	0.869±0.003	0.846±0.003	0.877±0.003
Prediction Accuracy CV	0.863±0.001	0.836±0.001	0.868±0.001
Positive Precision TS	0.918±0.012	0.916±0.012	0.930±0.011
Positive Precision CV	0.912±0.006	0.905±0.006	0.922±0.006
Negative Precision TS	0.746±0.029	0.677±0.032	0.746±0.029
Negative Precision CV	0.739±0.015	0.661±0.016	0.729±0.015
Matthews Correl. Coeff. TS	0.674±0.007	0.615±0.007	0.693±0.007
Matthews Correl. Coeff. CV	0.659±0.003	0.585±0.003	0.667 ±0.003

Table 4 Statistical metrics for classification of cancer/non-cancer using RF for normalised first derivative spectra

Metric	900-1800 cm^{-1}	2400-4000 cm^{-1}	Both
Sensitivity TS	0.918±0.011	0.897±0.013	0.912±0.012
Sensitivity CV	0.918±0.006	0.887±0.007	0.912±0.006
Specificity TS	0.883±0.022	0.820±0.027	0.875±0.023
Specificity CV	0.839±0.013	0.793±0.015	0.853±0.013
Prediction Accuracy TS	0.909±0.003	0.877±0.003	0.902±0.003
Prediction Accuracy CV	0.897±0.001	0.863±0.001	0.897±0.001
Positive Precision TS	0.957±0.008	0.937±0.010	0.957±0.008
Positive Precision CV	0.941±0.005	0.928±0.005	0.948±0.005
Negative Precision TS	0.795±0.027	0.730±0.030	0.769±0.028
Negative Precision CV	0.785±0.014	0.698±0.015	0.768±0.014
Matthews Correl. Coeff. TS	0.776±0.007	0.691±0.008	0.755±0.008
Matthews Correl. Coeff. CV	0.742±0.002	0.653±0.003	0.740±0.003

Table 5 Statistical metrics for classification of cancer/non-cancer using RF for normalised second derivative spectra

Metric	900-1800 cm^{-1}	2400-4000 cm^{-1}	Both
Sensitivity TS	0.928±0.011	0.825±0.015	0.923±0.011
Sensitivity CV	0.929±0.005	0.823±0.008	0.922±0.006
Specificity TS	0.915±0.019	0.766±0.035	0.914±0.018
Specificity CV	0.888±0.011	0.730±0.018	0.892±0.011
Prediction Accuracy TS	0.924±0.002	0.813±0.03	0.921±0.002
Prediction Accuracy CV	0.918±0.001	0.805±0.001	0.914±0.001
Positive Precision TS	0.970±0.007	0.937±0.010	0.970±0.007
Positive Precision CV	0.960±0.004	0.929±0.005	0.963±0.004
Negative Precision TS	0.812±0.026	0.511±0.034	0.804±0.026
Negative Precision CV	0.813±0.013	0.491±0.017	0.792±0.014
Matthews Correl. Coeff. TS	0.811±0.006	0.513±0.008	0.805±0.006
Matthews Correl. Coeff. CV	0.795±0.002	0.481±0.003	0.784±0.002

3.2 Spectral Features

Table 6 gives an overview of the identified wavenumber ranges in order of importance, together with their regions in the IR spectrum for second derivative data. The column "ΣGini" in the table is a summation of the (average over 96 RF classifications) mean decrease in Gini for each wavenumber within a given range. The most prominent ranges in terms of RF importance are the carbohydrate region at 997-1003 cm^{-1}, the phosphate region at 1290-1294 cm^{-1} and the lipid region at 1462-1464 cm^{-1}. These areas of importance are closely followed by other carbohydrate and protein modes.

Table 6 Identified important wavenumber ranges for the second derivative RF. The ranges are presented in order of decreasing importance to the classification.

Wavenumber Range	ΣGini	Tentative Assignment
997-1003 cm^{-1}	131.8	Carbohydrate
1290-1294 cm^{-1}	93.1	Phosphate
1462-1464 cm^{-1}	78.7	Lipid CH$_2$
1527-1533 cm^{-1}	71.9	Amide II
1028-1034 cm^{-1}	59.8	Carbohydrate
1387-1390 cm^{-1}	46.7	Protein COO$^-$
1194-1198 cm^{-1}	41.9	
1373-1377 cm^{-1}	39.9	Protein COO$^-$
1080-1082 cm^{-1}	31.4	Phosphate
1280-1282 cm^{-1}	28.6	
1093-1095 cm^{-1}	24.0	

Figures 3, 4, 5 & 6 show the mean decrease in Gini coefficient for all wavenumbers in a range, alongside generalised 2D correlation plots for the same data. In the 2D correlation plots, cancer spectra are on the horizontal axis, and non-cancer spectra are on the vertical. Data for the generalised 2D correlational analysis were obtained by averaging subsections of intensities in the dataset. In the figures showing the 2D correlation of the second derivative spectra, the averages were as follows: Figure 3: Synchronous spectrum of the average of all cancer spectra in the range 900-1800cm^{-1} vs all non-cancer spectra in the same range. Figures 4, 5 & 6 use the same pattern of average intensities of cancer and non-cancer spectra in the same wavenumber range, for both synchronous and asynchronous 2D plots. In the E.S.I., Figures S4 to S11 show similar plots for normalised and first derivative data. Figures S12 to S14 show average cancer and non-cancer spectra plotted together with Gini importance for normalised, first and second derivative spectra.

Usually when these 2D plots are generated, an incremental variable is used for the perturbation between the two sides of the correlation (eg temperature, pressure etc). In the case of this work, the perturbation is whether the patient has cancer or a normal diagnosis. It should also be borne in mind that the two inputted comparison spectra were averages of the whole class; i.e. Cancer and non-cancer. However, some information can still be
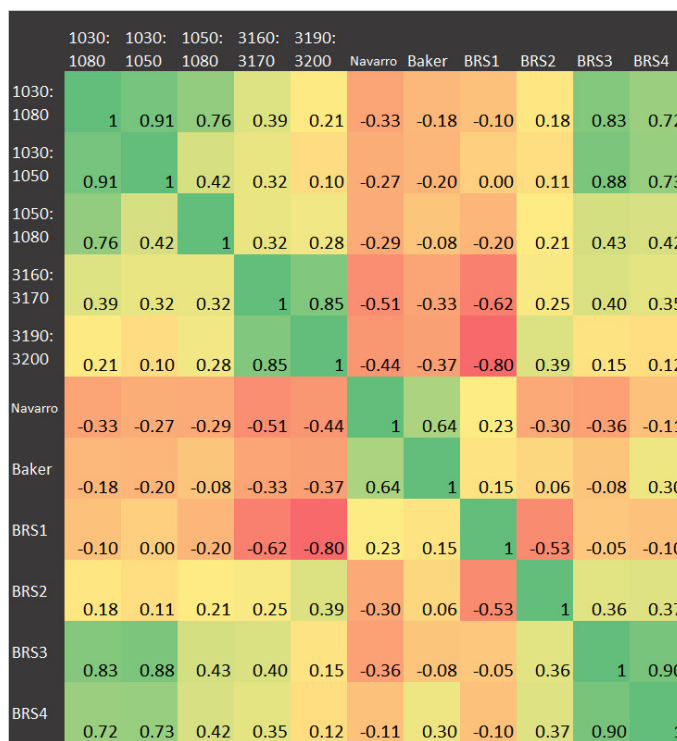
gleaned from Noda's method in this scenario. The synchronous spectrum shows whether two wavenumber ranges increase or decrease in intensity in the same or opposite directions. This is as normal for a synchronous generalised 2D correlation plot. The asynchronous spectrum is more subtle in its interpretation with a correlation such as this. Noda's Rules[44] show whether an intensity change occurs before or after another, with an incremental increase of some outside perturbation. There is no such incremental increase of a perturbation in this work, only a binary cancer/non-cancer descriptor. Therefore, the asynchronous plots serve as extra clarification to further highlight differences in the averaged spectra, without the influence of auto peaks. This therefore can provide a better means to identify major regions of the spectra which are responsible for the cancer/non-cancer distinction.

In Figures 3 & 4, it can be seen that the peaks at around 1640 and 1530 cm^{-1} show a strong correlation with each other. Only the peak centred around 1530 cm^{-1} appears as a strong spike in the RF classification. However, these two peaks are themselves correlated to other wavenumber ranges which are heavily featured in the RF study. In Figures 5 & 6, a similar situation can be seen with the two cross-peaks around the 2850 and 2930 cm^{-1} areas. This time however, both of these peaks also show strong peaks in the mean decrease in Gini.

The coupling together of the RF importance charts and the 2D correlations is helpful for further clarification of where the differences in the spectra lie, and whether these are reproduced in both studies. Another helpful piece of information from this is whether the major features of the RF importance charts match up to areas of major difference in intensities at certain wavenumbers. This allows further characterisation of the RF results, and gives clues as to whether minor or major differences in spectra are responsible for the greatest discrimination. Overall, the RF and 2D correlations are showing the same features via very different analyses, providing us further confidence due to the use of orthogonal techniques.

3.3 Ratiometrics

Fig. 7 Pearson Correlation Matrix of ratios taken from the raw data

	1030: 1080	1030: 1050	1050: 1080	3160: 3170	3190: 3200	Navarro	Baker	BRS1	BRS2	BRS3	BRS4
1030: 1080	1	0.91	0.76	0.39	0.21	-0.33	-0.18	-0.10	0.18	0.83	0.72
1030: 1050	0.91	1	0.42	0.32	0.10	-0.27	-0.20	0.00	0.11	0.88	0.73
1050: 1080	0.76	0.42	1	0.32	0.28	-0.29	-0.08	-0.20	0.21	0.43	0.42
3160: 3170	0.39	0.32	0.32	1	0.85	-0.51	-0.33	-0.62	0.25	0.40	0.35
3190: 3200	0.21	0.10	0.28	0.85	1	-0.44	-0.37	-0.80	0.39	0.15	0.12
Navarro	-0.33	-0.27	-0.29	-0.51	-0.44	1	0.64	0.23	-0.30	-0.36	-0.11
Baker	-0.18	-0.20	-0.08	-0.33	-0.37	0.64	1	0.15	0.06	-0.08	0.30
BRS1	-0.10	0.00	-0.20	-0.62	-0.80	0.23	0.15	1	-0.53	-0.05	-0.10
BRS2	0.18	0.11	0.21	0.25	0.39	-0.30	0.06	-0.53	1	0.36	0.37
BRS3	0.83	0.88	0.43	0.40	0.15	-0.36	-0.08	-0.05	0.36	1	0.90
BRS4	0.72	0.73	0.42	0.35	0.12	-0.11	0.30	-0.10	0.37	0.90	1

A Pearson correlation study was carried out on the ratios identified in the Materials and Methods section. Of particular interest from this correlational analysis of wavenumber ratios is the strong anti-correlation between BRS1 and 3190:3200 cm^{-1}. This may suggest a linked ratio apparent in our dataset, which spans a wide range from the Amide regions to the hydrogen bonding region. Ratio pairs from wavenumber ranges located near to each other on the spectrum generally had a strong positive correlation, for example those at 1030:1050 cm^{-1} and 1050:1080 cm^{-1}. An anti-correlation is noted the pair 3160:3170 cm^{-1} and BRS1. BRS3 and BRS4 also exhibit a strong correlation; both ratios being a carbohydrate:lipid type at different wavenumber ranges. The result of 0.00 for 1030:1050 cm^{-1} vs BRS1 is interesting, as this suggests that the ratio of intensities of AmideI:AmideII and those of the carbohydrate region vary completely independently of one another. The adjacent carbohydrate ratios of 1030:1080 cm^{-1} and 1050:1080 cm^{-1} also show a very low correlation with the AmideI:AmideII ratio.

It was found that the 900-1800 cm^{-1} range of the spectral data produced the greatest accuracy for RF. The higher end of the spectrum from 2400-4000 cm^{-1} performed adequately alone, but did not add to the accuracy of the classification when used alongside 900-1800 cm^{-1}. This suggests a correlation between the upper

and lower ends of the spectrum, as evidenced also in the ratio correlation graphic (Fig. 7). The lower end therefore represents a better option, as the calculation is less expensive than using the full range. In the work leading up to these results, the first derivative spectra were found to be intermediate between raw data and the second derivative in terms of statistical results and clarity of important wavenumbers. The results of the generalised 2D correlational analysis proved to be useful as a comparison to the RF results. It allowed for better visualisation of the differences in spectra and tallied well (as expected) with the importance charts. Our method works well for the binary classification of cancer/non-cancer, the next step would be to develop further the classification of disease states within the cancer subset.

4 Conclusions

Significant differences in IR spectra of differing disease states were observed in this study, and we have proven that our approach has potential in the area of cancer diagnosis. We have employed and thoroughly tested the random forest technique and its associated Gini feature importance, and proven it to be effective in classifying cancer and non-cancer states. Noda's generalised 2D IR approach has proven to be a useful adjunct in verifying the importance results from RF. A robust pre-processing regimen was also developed in the course of this work; it was found that the normalised second derivative of the spectral data was most effective in our RF classification. Investigation of various spectral ratios was also carried out. While not immediately useful in RF classification, some new relationships between ratios were found which may prove interesting in further studies.

This research has shown a rapid, computationally light, accurate, statistically robust methodology for the identification of spectral features that define a dataset. The identification of these features is in line with Occam's razor and supports accurate diagnostics by focusing upon salient information as opposed to including information from biological variance within the diagnosis. With current advances in IR technology, such as the development of rapid discrete frequency collection, this approach is of importance to enable future clinical translation and enables IR to achieve its potential.

5 Acknowledgements

References

1 W. H. Organization *et al.*, *WHO Report. Geneva: WHO*, 2014.

2 ONS, *Cancer Statistics Registrations, England*, http://www.ons.gov.uk/ons/rel/vsob1/cancer-statistics-registrations--england--series-mb1-/no--41--2010/cancer-statistics-registrations--england--series-mb1----no--41--2010--statistical-bulletin.html, 2010, Accessed: 23-09-2015.

3 M. Wrensch, Y. Minn, T. Chew, M. Bondy and M. S. Berger, *Neuro-oncology*, 2002, **4**, 278–299.

4 N. Burnet, S. Jefferies, R. Benson, D. Hunt and F. Treasure, *Br. J. Cancer*, 2005, **92**, 241–245.

5 C. R. UK, *Statistics and outlook for brain tumours*, http://www.cancerresearchuk.org/about-cancer/type/brain-tumour/treatment/statistics-and-outlook-for-brain-tumours, 2015, Accessed: 23-09-2015.

6 J. R. Hands, K. M. Dorling, P. Abel, K. M. Ashton, A. Brodbelt, C. Davis, T. Dawson, M. D. Jenkinson, R. W. Lea, C. Walker *et al.*, *J. Biophotonics*, 2014, **7**, 189–199.

7 B. R. Trust, *About Brain Tumours*, http://www.brt.org.uk/brain-tumours, Accessed: 23-09-2015.

8 C. R. UK, *Primary and Secondary Brain Tumours*, http://www.cancerresearchuk.org/about-cancer/type/brain-tumour/about/primary-and-secondary-brain-tumours, 2015, Accessed: 23-09-2015.

9 R. Soffietti, A. Ducati and R. Rudà, *Handb. Clin. Neurol.*, 2012, **105**, 747–55.

10 NICE, *Suspected cancer: recognition and referral*, http://www.nice.org.uk/guidance/NG12/chapter/1-recommendations#brain-and-central-nervous-system-cancers, 2015, Accessed: 23-09-2015.

11 D. J. Brenner and E. J. Hall, *N. Engl. J. Med.*, 2007, **357**, 2277–2284.

12 M. S. Pearce, J. A. Salotti, M. P. Little, K. McHugh, C. Lee, K. P. Kim, N. L. Howe, C. M. Ronckers, P. Rajaraman, A. W. Craft *et al.*, *Lancet*, 2012, **380**, 499–505.

13 J. M. Bruner, L. Inouye, G. N. Fuller and L. A. Langford, *Cancer*, 1997, **79**, 796–803.

14 N. C. I. Network, *routes to diagnosis*, http://www.ncin.org.uk/publications/routes_to_diagnosis, 2010, Accessed: 23-09-2015.

15 N. C. I. Network, *data briefings/routes to diagnosis*, http://www.ncin.org.uk/publications/data_

briefings/routes_to_diagnosis, 2010, Accessed: 23-09-2015.

16 M. H. via The Brain Tumour Charity, *Finding a better way?*, http://www.thebraintumourcharity. org/Resources/SDBTT/news/documents/ the-brain-tumour-charity-report-on-improving -quality-of-life-final-report-dec2013.pdf, 2013, Accessed:23-09-2015.

17 A. S. Haka, K. E. Shafer-Peltier, M. Fitzmaurice, J. Crowe, R. R. Dasari and M. S. Feld, *P. Natl. Acad. Sci. USA*, 2005, **102**, 12371–12376.

18 V. R. Kondepati, H. M. Heise and J. Backhaus, *Anal. Bioanal. Chem.*, 2008, **390**, 125–139.

19 J. Pichardo-Molina, C. Frausto-Reyes, O. Barbosa-García, R. Huerta-Franco, J. González-Trujillo, C. Ramírez-Alvarado, G. Gutiérrez-Juárez and C. Medina-Gutiérrez, *Laser. Med. Sci.*, 2007, **22**, 229–236.

20 J. Backhaus, R. Mueller, N. Formanski, N. Szlama, H.-G. Meerpohl, M. Eidt and P. Bugert, *Vib. Spectrosc.*, 2010, **52**, 173–177.

21 K. Gajjar, J. Trevisan, G. Owens, P. J. Keating, N. J. Wood, H. F. Stringfellow, P. L. Martin-Hirsch and F. L. Martin, *Analyst*, 2013, **138**, 3917–3926.

22 J. R. Hands, P. Abel, K. Ashton, T. Dawson, C. Davis, R. W. Lea, A. J. McIntosh and M. J. Baker, *Anal. Bioanal. Chem.*, 2013, **405**, 7347–7355.

23 M. J. Baker, C. Clarke, D. Démoulin, J. Nicholson, F. M. Lyng, H. J. Byrne, C. A. Hart, M. D. Brown, N. W. Clarke and P. Gardner, *Analyst*, 2010, **135**, 887–894.

24 M. J. Baker, E. Gazi, M. D. Brown, J. H. Shanks, P. Gardner and N. W. Clarke, *Br. J. Cancer*, 2008, **99**, 1859–1866.

25 E. Gazi, M. Baker, J. Dwyer, N. P. Lockyer, P. Gardner, J. H. Shanks, R. S. Reeve, C. A. Hart, N. W. Clarke and M. D. Brown, *Eur. Urol.*, 2006, **50**, 750–761.

26 L. Li, H. Tang, Z. Wu, J. Gong, M. Gruidl, J. Zou, M. Tockman and R. A. Clark, *Artificial intelligence in medicine*, 2004, **32**, 71–83.

27 M. R. Kole, R. K. Reddy, M. V. Schulmerich, M. K. Gelber and R. Bhargava, *Anal. Chem.*, 2012, **84**, 10366–10372.

28 B. Bird and M. J. Baker, *Trends Biotechnol.*, 2015, **33**, 557–558.

29 K. M. Dorling and M. J. Baker, *Appl. Environ. Microbiol*, 2013, **74**, 3868–3876.

30 L. Lovergne, G. Clemens, V. Untereiner, R. A. Lukaszweski, G. D. Sockalingum and M. J. Baker, *Anal. Methods*, 2015.

31 I. Noda, *Appl. Spectrosc.*, 1993, **47**, 1329–1336.

32 N. T. Hunt, *Chem. Soc. Rev.*, 2009, **38**, 1837–1848.

33 MATLAB, *version 8.5.0 (R2015a)*, The MathWorks Inc., Natick, Massachusetts, 2015.

34 E. Gazi, J. Dwyer, P. Gardner, A. Ghanbari-Siahkali, A. Wade, J. Miyan, N. P. Lockyer, J. C. Vickerman, N. W. Clarke, J. H. Shanks *et al.*, *J. Pathol.*, 2003, **201**, 99–108.

35 P. Bassan, J. Mellor, J. Shapiro, K. J. Williams, M. P. Lisanti and P. Gardner, *Anal. Chem.*, 2014, **86**, 1648–1653.

36 S. Navarro, D. Borchman and E. Bicknell-Brown, *Anal. Biochem.*, 1984, **136**, 382–389.

37 M. J. Baker, J. Trevisan, P. Bassan, R. Bhargava, H. J. Butler, K. M. Dorling, P. R. Fielden, S. W. Fogarty, N. J. Fullwood, K. A. Heys *et al.*, *Nat. Protoc.*, 2014, **9**, 1771–1791.

38 L. Breiman, *Mach. Learn.*, 2001, **45**, 5–32.

39 A. Liaw and M. Wiener, *R news*, 2002, **2**, 18–22.

40 D. S. Palmer, N. M. O'Boyle, R. C. Glen and J. B. O. Mitchell, *J. Chem. Inf. Model.*, 2007, **47**, 150–158.

41 L. D. Hughes, D. S. Palmer, F. Nigsch and J. B. Mitchell, *J. Chem. Inf. Model.*, 2008, **48**, 220–232.

42 D. S. Palmer, M. Mišin, M. V. Fedorov and A. Llinas, *Mol. Pharm.*, 2015, **12**, 3420–3432.

43 S. Morita, *2Dshige. Kwansei-Gakuin University*, 2004.

44 I. Noda, *J. Mol. Struct.*, 2006, **799**, 41–47.

6 E.S.I

Fig. S1 Average spectra for cancer and non-cancer, together with their standard deviations
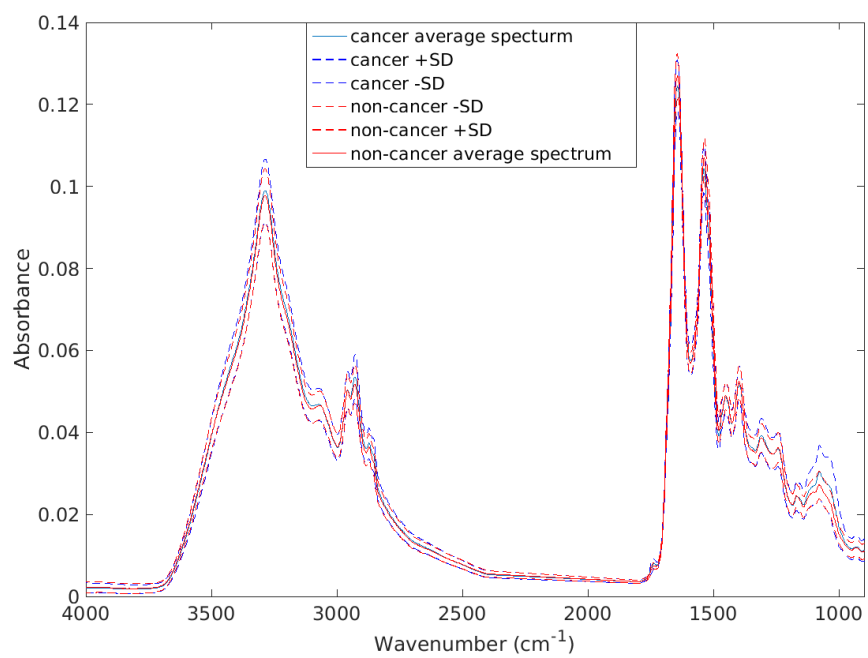
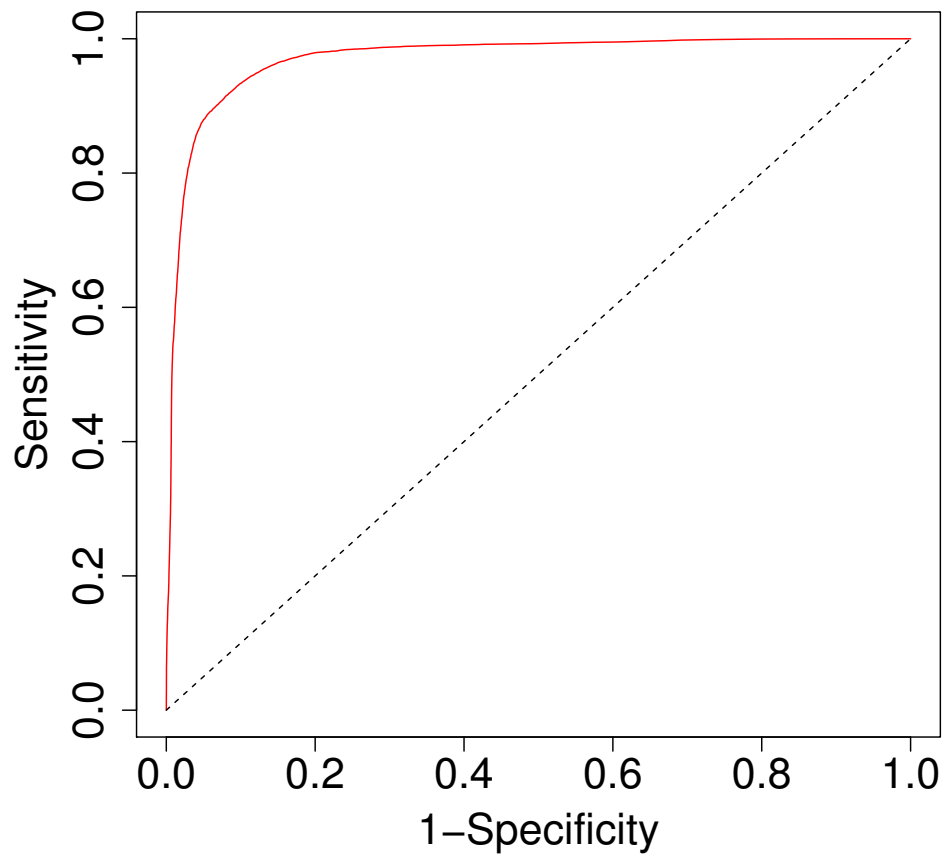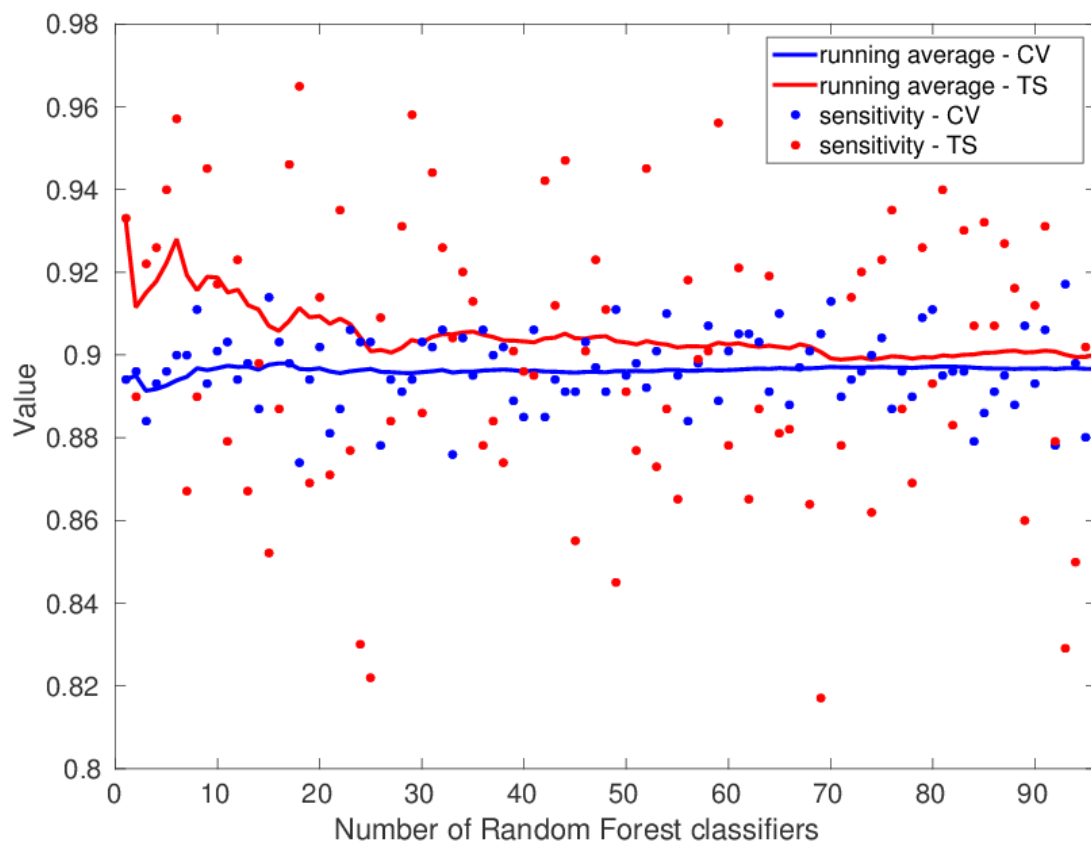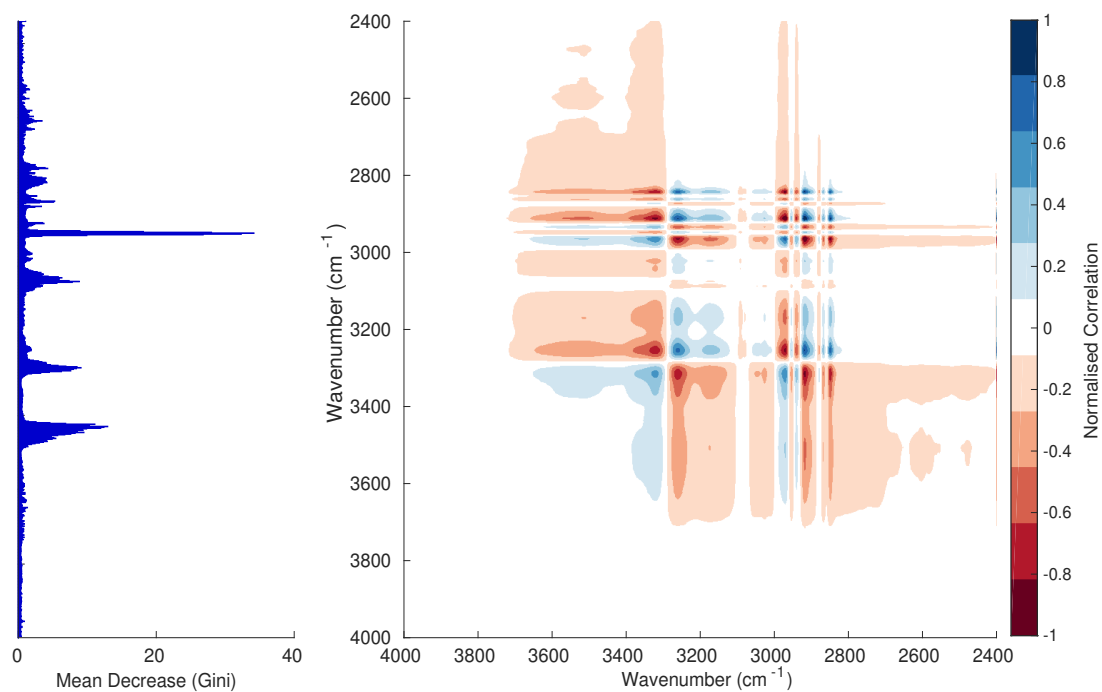**Fig. S2** Receiver Operator Curve from the second derivative 900-1800 cm^{-1} range

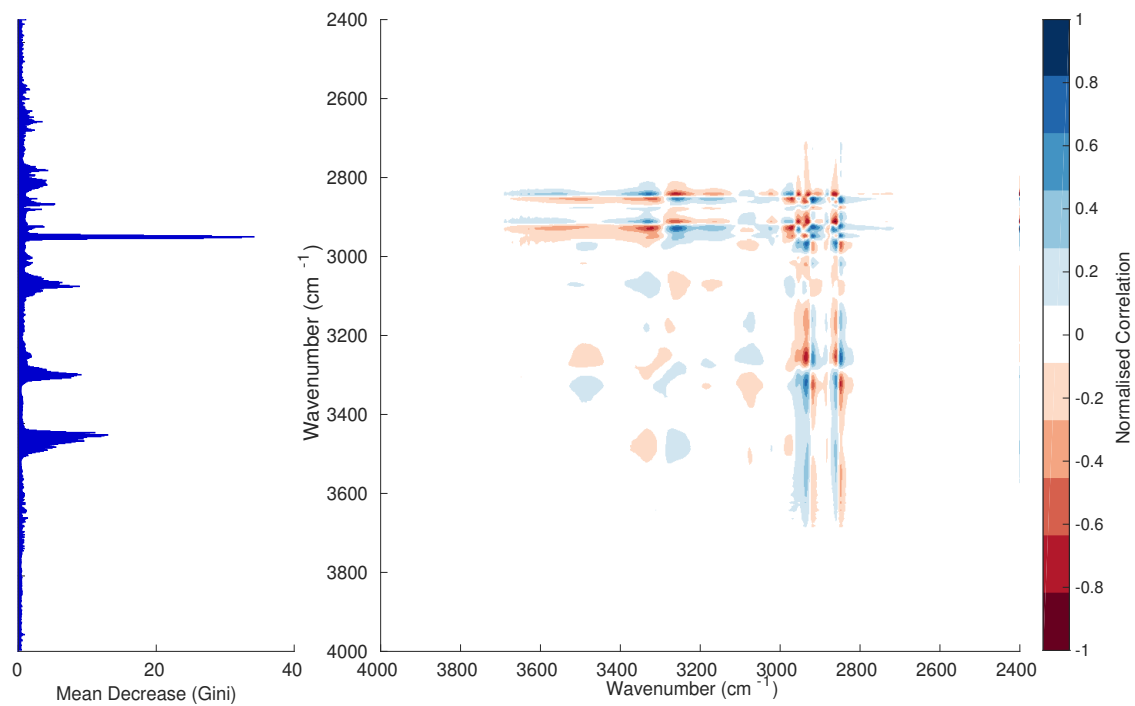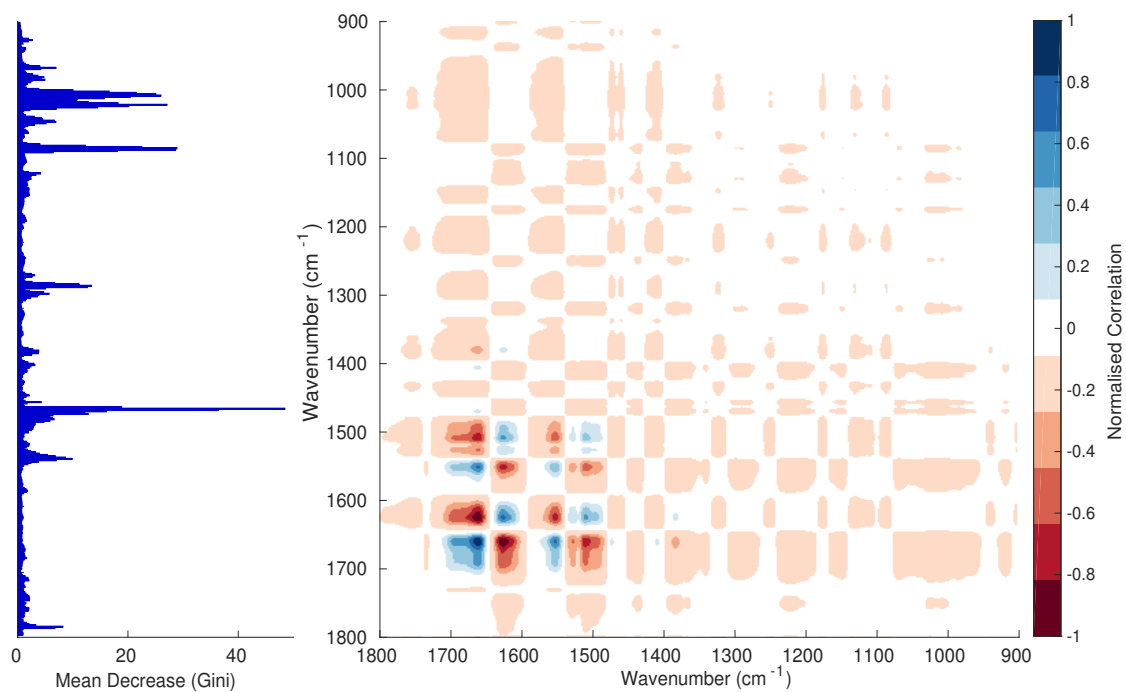**Fig. S3** Convergence of sensitivity w.r.t. number of RF models

Fig. S4 Gini Importance Chart - 2400-4000cm^{-1} First Derivative with Synchronous 2D plot

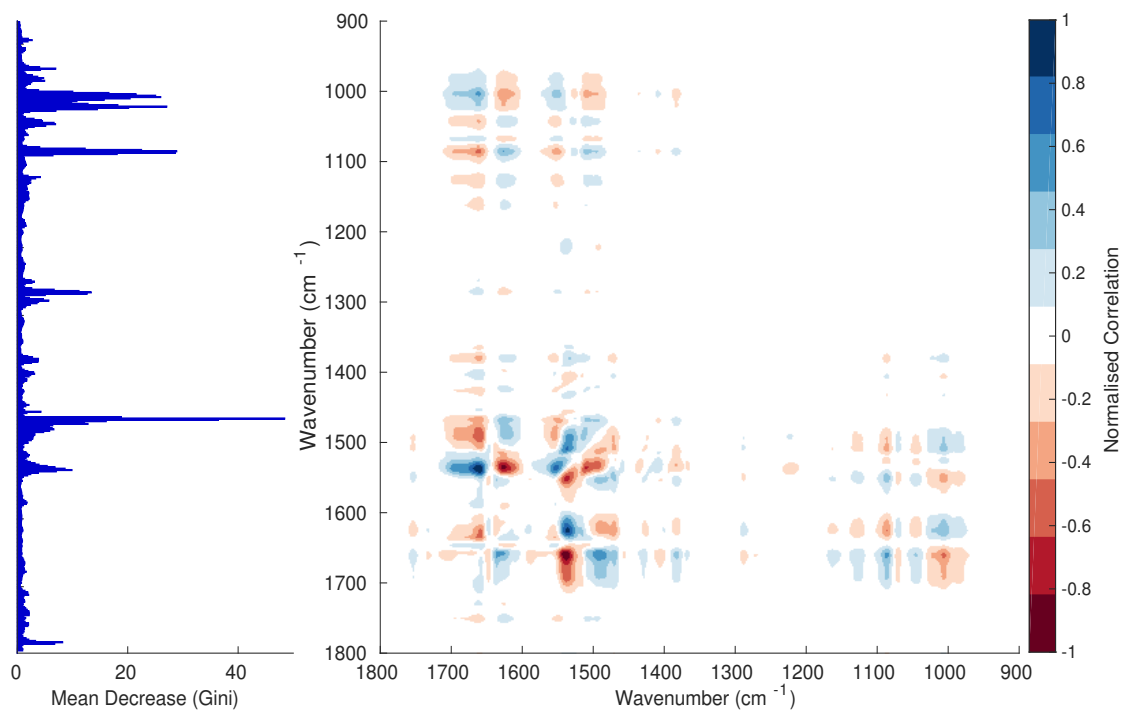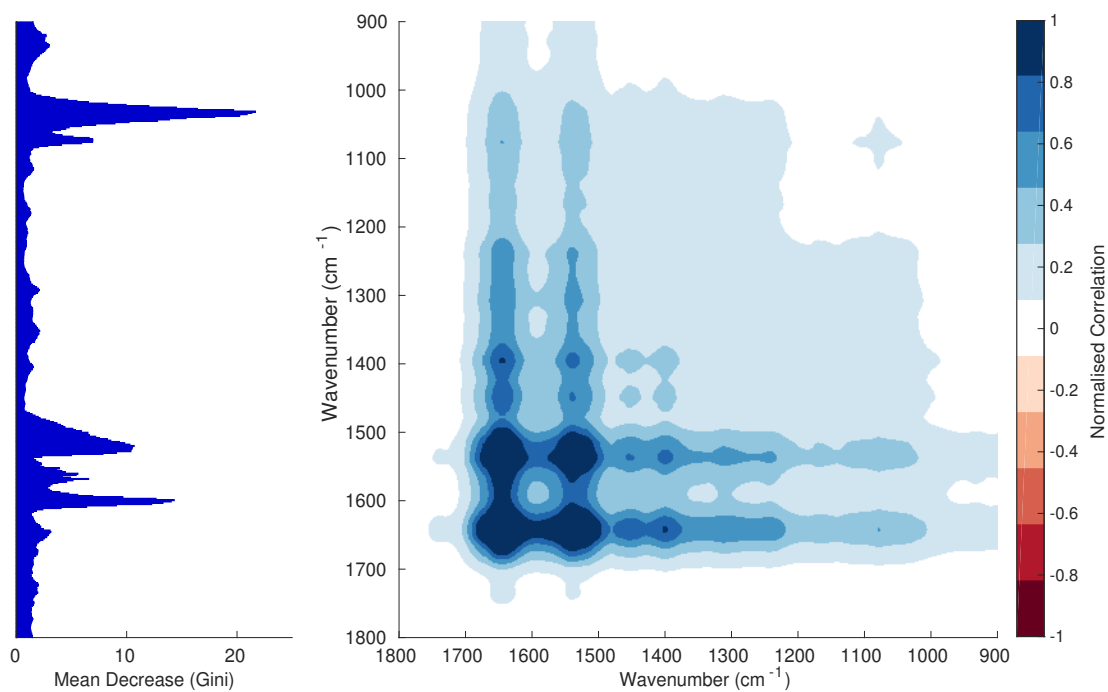**Fig. S5** Gini Importance Chart - 2400-4000cm^{-1} First Derivative with Asynchronous 2D plot

Fig. S6 Gini Importance Chart - 900-1800cm^{-1} First Derivative with Synchronous 2D plot

Fig. S7 Gini Importance Chart - 900-1800cm^{-1} First Derivative with Asynchronous 2D plot

Fig. S8 Gini Importance Chart - 900-1800cm^{-1} Normalised Spectra with Synchronous 2D plot

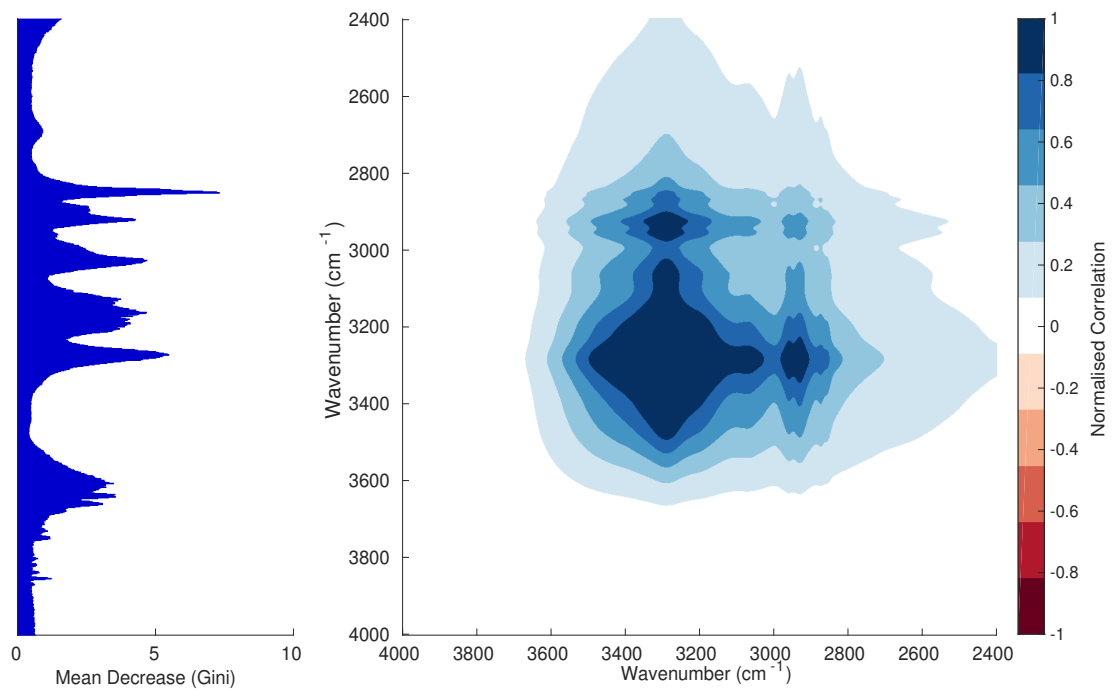**Fig. S9** Gini Importance Chart - 900-1800cm^{-1} Normalised Spectra with Asynchronous 2D plot
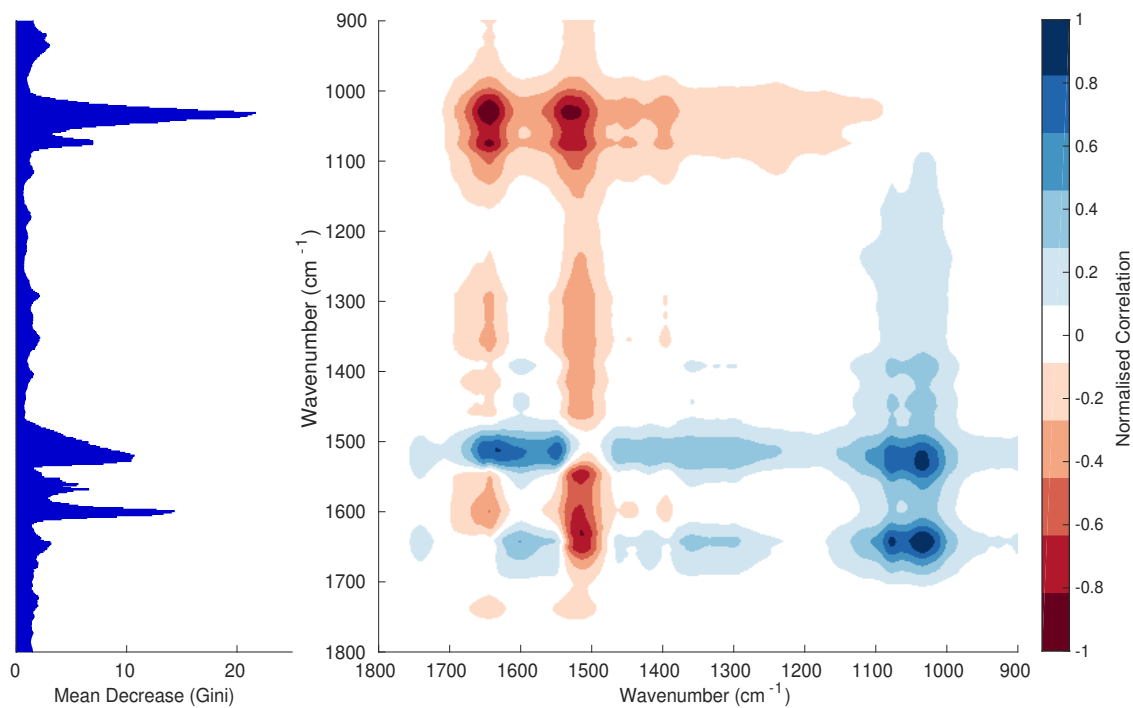
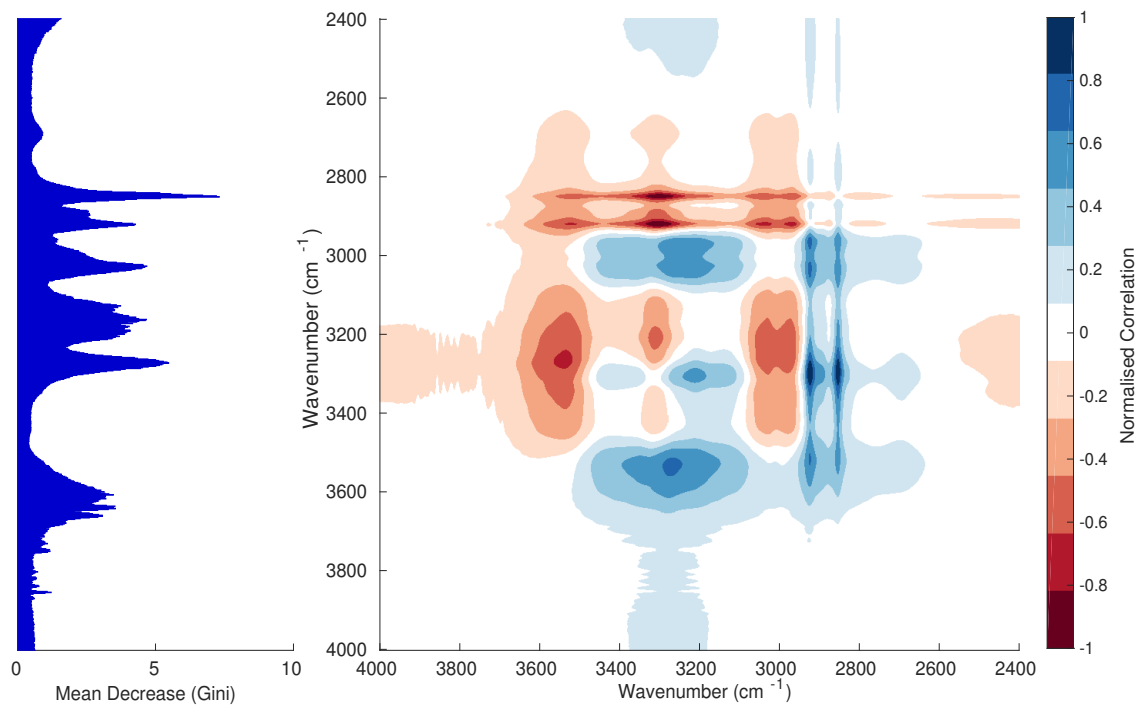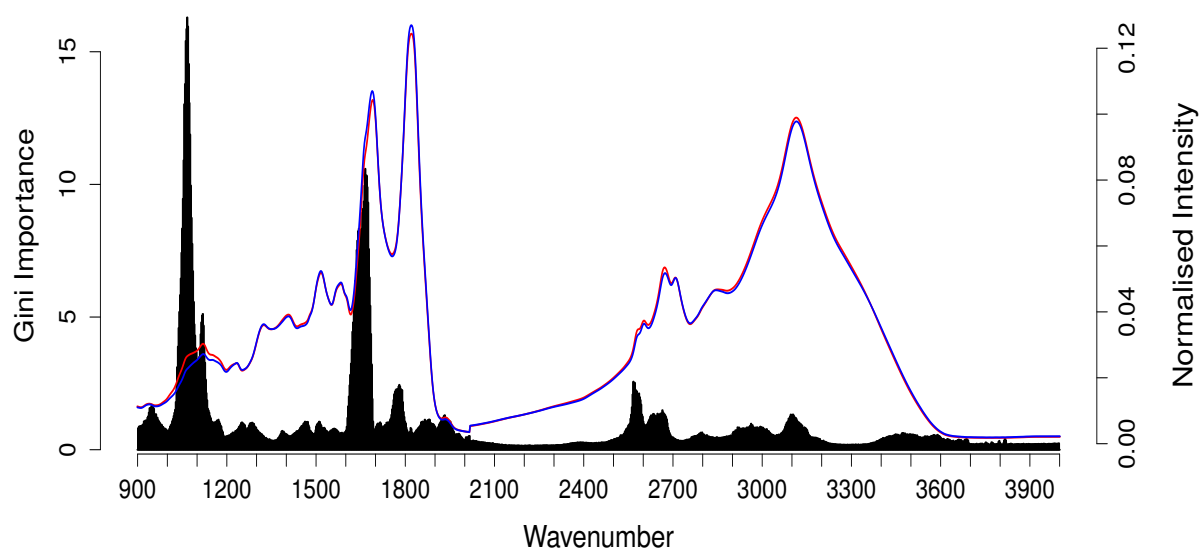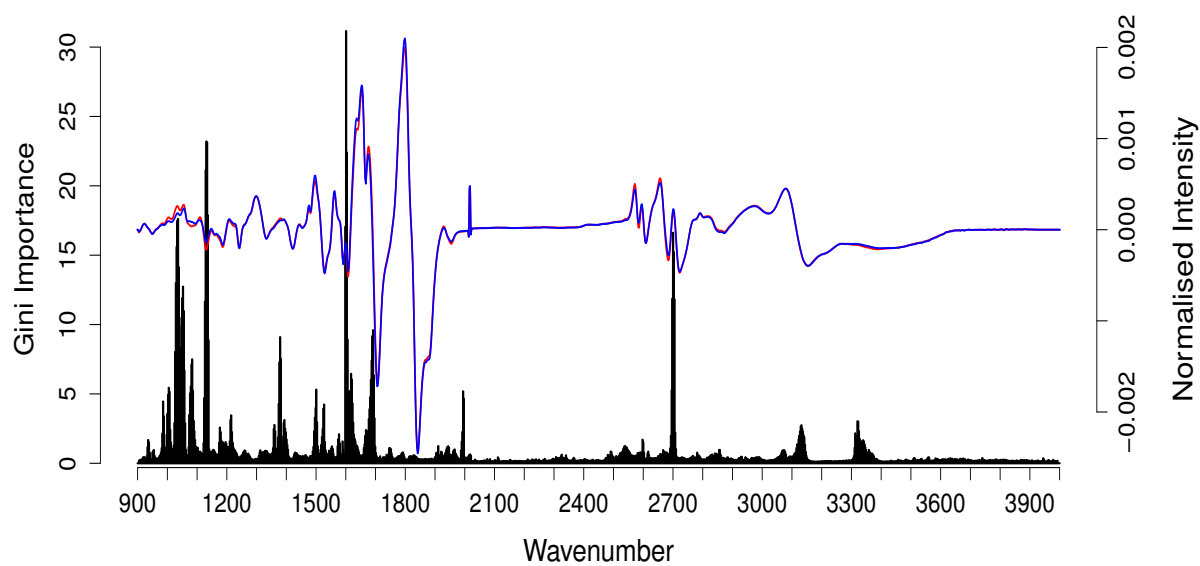**Fig. S10** Gini Importance Chart - 2400-4000cm^{-1} Normalised Spectra with Synchronous 2D plot

Fig. S11 Gini Importance Chart - 2400-4000cm^{-1} Normalised Spectra with Asynchronous 2D plot

Fig. S12 Gini Importance Chart - 900-4000cm^{-1} with average cancer (red) and non-cancer (blue) normalised spectra

Fig. S13 Gini Importance Chart - 900-4000cm^{-1} with average cancer (red) and non-cancer (blue) first derivative spectra

Fig. S14 Gini Importance Chart - 900-4000cm^{-1} with average cancer (red) and non-cancer (blue) second derivative spectra